3D interconnected hierarchically porous N-doped carbon with NH₃ activation for efficient oxygen reduction reaction

Yi Wang [a,*], Hanyu Liu [a], Kun Wang [b], Shuqin Song [b], Panagiotis Tsiakaras [c,d,**]

[a] The Key Lab of Low-carbon Chemistry & Energy Conservation of Guangdong Province, School of Chemical Engineering and Technology, Sun Yat-sen University, Zhuhai 519082, China
[b] School of Materials Science and Engineering, Sun Yat-sen University, Guangzhou 510275, China
[c] Laboratory of Alternative Energy Conversion Systems, Department of Mechanical Engineering, University of Thessaly, Pedion Areos, Volos 383 34, Greece
[d] Laboratory of Electrochemical Devices based on Solid Oxide Proton Electrolytes, Institute of High Temperature Electrochemistry, Yekaterinburg 620990, Russia

ABSTRACT

In the present work, a novel metal-free ORR electrocatalyst, with large specific surface area (2600 m² g⁻¹), high content of N dopants (3.12 at.%) and 3D cross-linking hierarchically porous structure (abbreviated as LHNHPC) is readily prepared by using a modified classical carbon-aerogel method with NH₃ as the activating agent.

Compared with benchmark Pt/C catalyst, it is found that, LHNHPC exhibits similar electrocatalytic activity towards oxygen reduction reaction (ORR), superior durability and excellent methanol tolerance in basic media. The above electrochemical properties of LHNHPC are mainly attributed to the synergistic contribution of its unique hierarchical pore structure, the rich N doping and the large surface area.

It can be anticipated that the proposed two-step process could be used for mass production of metal free electrocatalysts for a wide range of electrochemical devices including fuel cells and metal-air batteries.

© 2017 Elsevier B.V. All rights reserved.

1. Introduction

Along with the development of society and technology, our demand in energy is becoming surging [1–5]. Regular energies we employ nowadays are mostly non-recycled, which will be running out some day in the future. Therefore, hard working on research and development of new energy is an effective way to solve the problem of energy crisis [6–10]. Recently, many advanced technologies for electrochemical energy storage and conversion technologies including *fuel cells* (FCs), metal-air batteries and electrolysis cells have been widely discussed by academic and governmental organizations [11–14]. The core of these novel technologies consists of a series of electrochemical processes, which include electrocatalytic *oxygen reduction reaction* (ORR) that occurs at the cathode

with sluggish kinetics and high overpotential. Obviously, developing active and durable ORR electrocatalysts is crucial for successful implementation of these technologies [15,16].

FCs have attracted a great deal of attention due to their low operation temperature, environmental benignity, long life spans and so on [17,18]. One of the technical challenges for FCs is the undesirable ORR performance [19–24]. Pt or Pt-based alloys have been well acknowledged to be the most outstanding ORR electrocatalysts; however, their instability in acidic medium, CO deactivation and high cost of Pt, hinder their large-scale applications. Heteroatoms (N, S, B, P, F)-doped carbon materials, such as *carbon nanotubes* (CNTs) [25–33], graphene [34–36], graphitic arrays [37], and amorphous carbon [38–43], have been found to exhibit excellent electrocatalytic ORR performance. Dai's group proposed vertically aligned nitrogen-containing CNTs exhibiting excellent ORR activity by the transformation of O₂ adsorption due to N doping, providing a four-electron pathway for the ORR process [44]. Qiao's group proved that the superior ORR catalytic activity in alkaline media is due to the nitrogen dopants including quaternary-N, which is beneficial for the limiting current density, and pyridinic-N that could decrease the adsorption energy of O₂ at electrode surface resulting in a positive onset potential [45]. Also, Dai's group first reported N-doped graphene for ORR involving the

---

* Corresponding author at: The Key Lab of Low-carbon Chemistry & Energy Conservation of Guangdong Province, School of Chemical Engineering and Technology, Sun Yat-sen University, Zhuhai 519082, China.
** Corresponding author at: Laboratory of Alternative Energy Conversion Systems, Department of Mechanical Engineering, University of Thessaly, Pedion Areos, Volos 383 34, Greece.
E-mail addresses: wangyi76@mail.sysu.edu.cn (Y. Wang), tsiak@uth.gr, tsiakaras.fc@gmail.com (P. Tsiakaras).
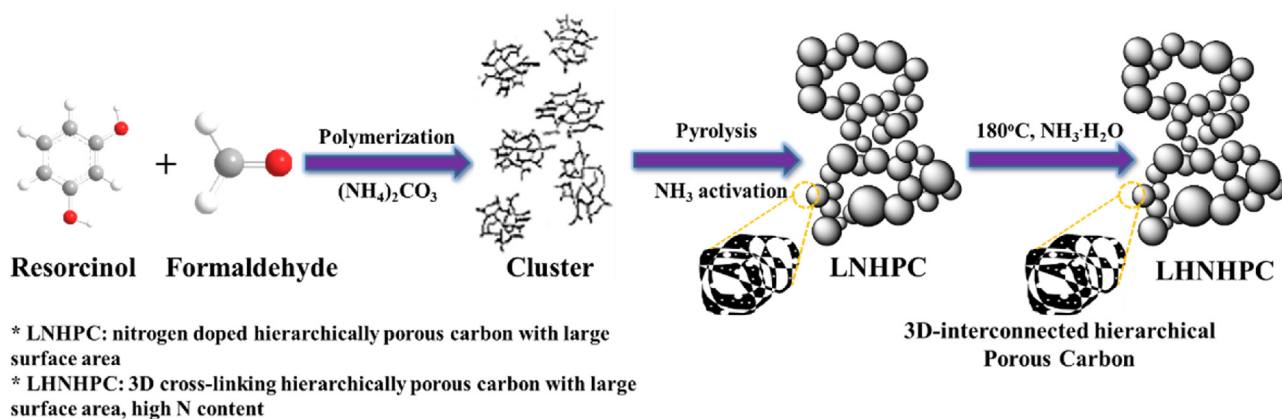
Fig. 1. The route for stepwise structural evolution from raw materials to LHNHPC.
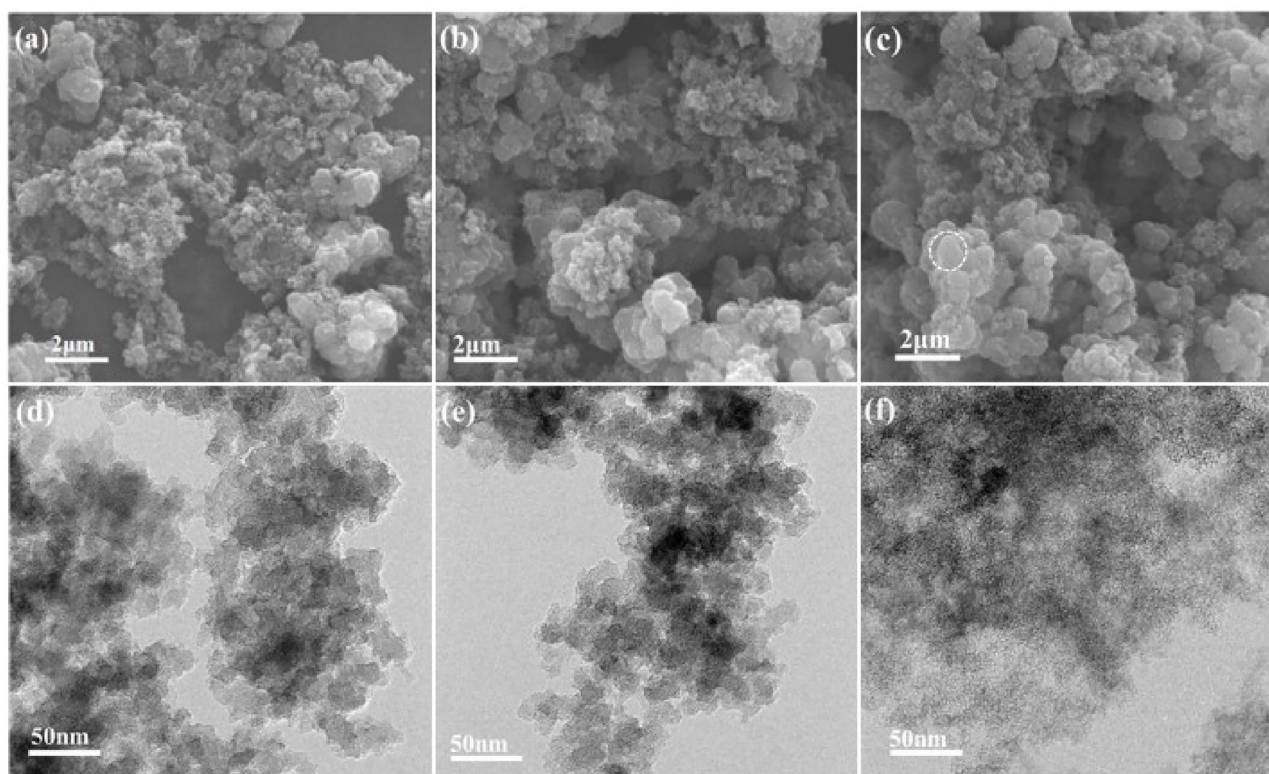

Fig. 2. Physical characterizations: SEM (a, b, c), and the corresponding TEM images (d, e, f) of LNHPC-800, LNHPC-900 and LNHPC-1000, respectively.

technology of chemical vapor deposition of methane in the presence of ammonia. This N-graphene material exhibited excellent ORR performance in basic media due to the large specific surface area of N-graphene films [46].

To make a metal-free ORR electrocatalyst truly competitive with Pt/C, three crucial factors governing the electrocatalytic performance of materials have to be simultaneously considered: (i) rich N doping and large specific surface area for amounts of accessible active sites, (ii) highly graphitization for excellent electrical conductivity, and (iii) properly hierarchical pore structure for rapid mass transfer. Lou et al. reported a novel type of ORR electrocatalyst derived from a metal-organic frameworks (MOFs), which displayed remarkable electrocatalytic activity and stability, and even outperformed a commercial Pt/C catalyst. This behavior was mainly attributed to the chemical composition and structure of the formed crystalline NCNTs, as well as their robust overall framework structure [47]. They also reported iron carbide nanoparticle-embedded carbon nanotube assemblies with a high ORR performance through a dual MOF confined-pyrolysis approach [48]. S and N co-doped mesoporous carbon could improve the ORR catalytic activity in alkaline media, owing to the synergistic effect from S and N and the large specific surface area [49,50]. Feng et al. discovered hierarchically porous carbons with optimized nitrogen doping and large specific surface area, which could simultaneously enhance the electron transfer rate and shorten the mass transfer pathway, and thus exhibit excellent ORR performance at a half-wave potential of 0.85 V (vs. RHE) (versus reversible hydrogen electrode) with a low catalyst loading of 0.1 mg cm^{-2} in alkaline media [51]. In spite of the tremendous progress, the improvement of ORR performance seems still the more fundamental issue that should be preferentially resolved and further investigated..
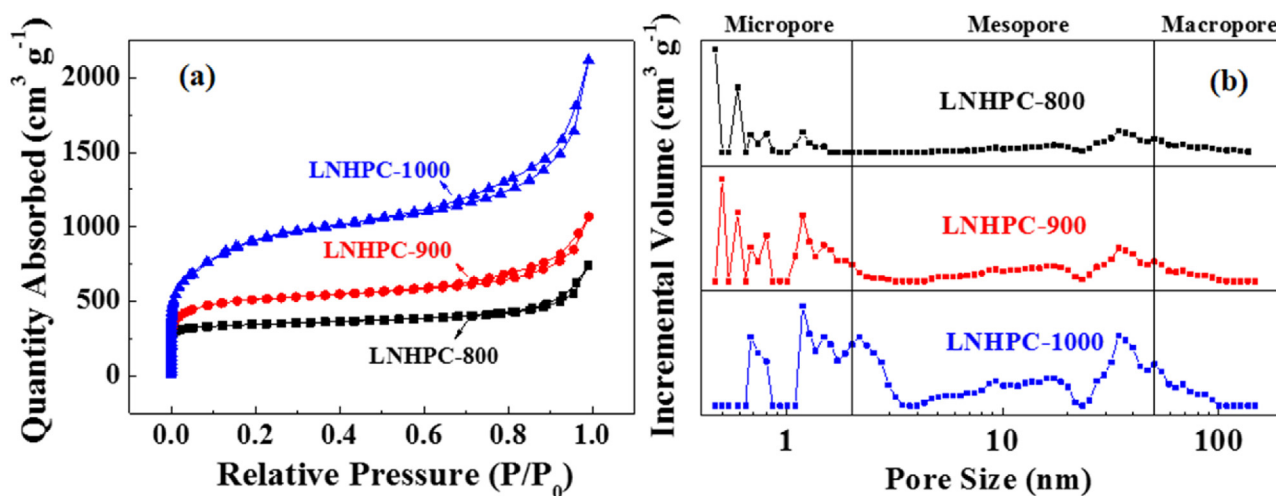
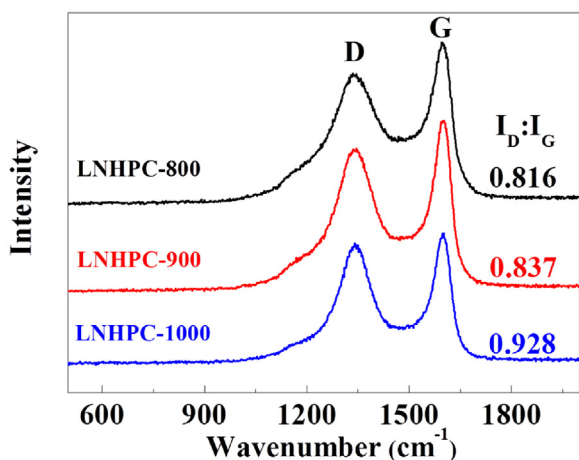**Fig. 3.** N$_2$ adsorption/desorption isotherms (a), and the corresponding pore size distribution of LNHPC-x (b).

Fig. 4. Raman spectra of LHNPC-x and their corresponding intensity ratio of D-band to G-band (I$_D$/I$_G$).

Herein, we report a simple two-step process to synthesize a new type of metal-free ORR electrocatalyst; a *3D cross-linking hierarchically porous carbon with large surface area, and highcontent* (LHNHPC), possessing large specific surface area, abundant active sites for ORR (PyridinicN), and hierarchical porous structure with a multimodal pore distribution for rapid mass transfer, and consequently exhibiting high ORR activity, superior long-term stability and excellent methanol tolerance performance compared with the commercial Pt-based ORR electrocatalysts.

2. Experimental section

2.1. Materials

Resorcinol and aqueous ammonia were purchased from Tianjin Chemical Reagent Co., China. Ammonium carbonate was obtained from Shanghai Aladdin, China. Formaldehyde was purchased from Guangzhou Chemical Reagent Co., China. All chemical reagents were of analytical grade and used without any further purification.

2.2. Synthesis and characterization

The route for stepwise structural evolution from raw materials to LHNHPC is schematically shown below in Fig. 1.

LNHPC (nitrogen doped hierarchically porous carbon with large surface area) was readily available by the reaction of resorcinol and formaldehyde in the presence of ammonium carbonate as reported everywhere [52]. In the first step, 40.0 mL deionized water, 28.0 mL ethanol and 1.5 mL aqueous ammonia were mixed in a 100 mL of beaker, followed by being stirred for 10 min to make them fully dissolved. The mixture was then transferred into a 150 mL three-necked flask and immersed in a constant-temperature water bath at 30 °C. In the second step, 0.3 g resorcinol, 0.42 mL formaldehyde and 1.0 g ammonium carbonate were added into the reaction, and this mixture was stirred in the container for 24 h. Then, the solution was transferred into a Teflon-lined stainless-steel autoclave (100 mL). The sealed autoclave was heated in an electric oven at 100 °C for 24 h, and then allowed to cool down slowly at room temperature. In the third step, the brown precipitate was collected by centrifugation, washed with ethanol several times and dried under vacuum at 80 °C. Target materials were attained by the pyrolysis process at various temperatures (800, 900, and 1000 °C) for 3 h in NH$_3$ atmosphere at a heating rate of 5 °C min^{-1} and then directly cooled naturally down to room temperature. The as-prepared samples are denoted as LNHPC-x (x represents the pyrolysis temperature). All carbon samples were treated under vacuum at 80 °C for 10 h before being used for the further electrochemical study. In order to synthesize the LHNHPC samples, aqueous ammonia was added and a hydrothermal reaction was proceeded at 180 °C for 12 h with LNHPC-1000 as a precursor. The as-prepared black powder was collected by centrifugation, repeatedly washed with DI water, and then dried at 80 °C under vacuum.

2.3. Physicochemical characterization

The morphology of the samples was investigated using a *scanning electron microscope* (SEM, FEI Quanta 400) and *transmission electron microscope* (TEM, JEOL JEM-2010HR). The composition of the samples was analyzed using *X-ray photoelectron spectroscopy* (XPS, VG Scientific ESCALAB250) equipped with Al Kα X-ray source (1486.6 eV). The obtained spectrograms were analyzed with Xps-peak41 software. The nitrogen adsorption/desorption experiments were performed on Micromeritics ASAP2020. Before the measurements, the samples were dried at 250 °C for more than 8 h under vacuum conditions. The specific surface area was calculated by using *Brunauer-Emmett-Teller* (BET) analysis. Raman spectroscope analysis was conducted by Renishaw in *Via* Laser Micro-Raman Spectrometer to study the graphitic nature of LNHPC-x. Elemental
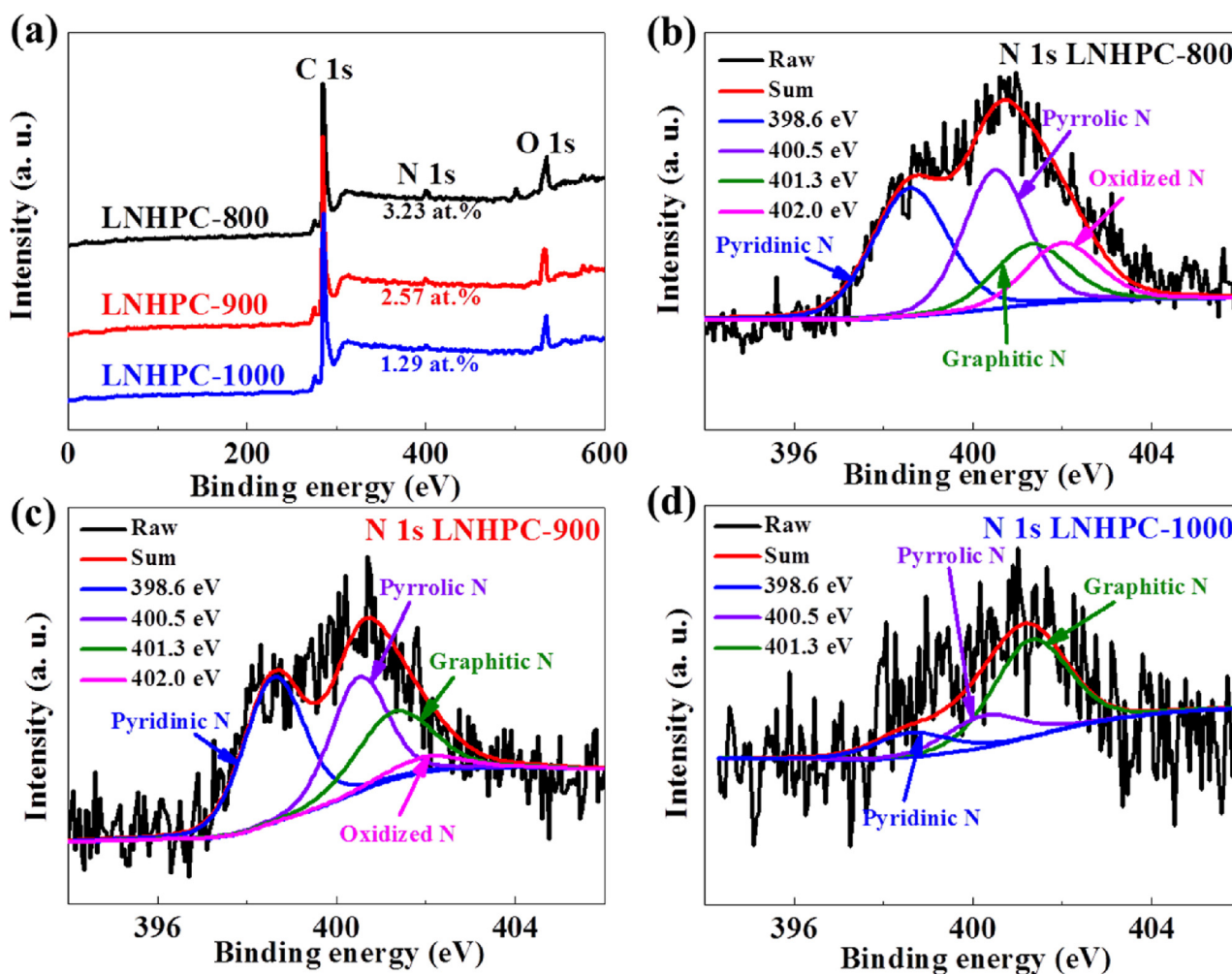
Fig. 5. XPS survey spectra of the HNHPC-x (a); the high resolution N1s XPS spectra of LNHPC-800 (b), LNHPC-900 (c) and LNHPC-1000 (d), respectively.
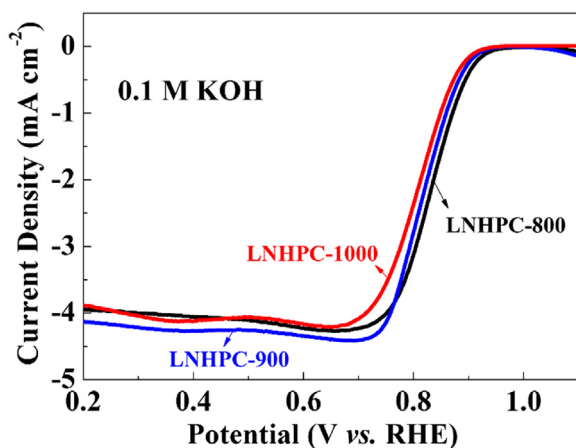

Fig. 6. RDE polarization curves of LNHPC-800, LNHPC-900 and LNHPC-1000 in O_2-saturated 0.1 mol L^{-1} KOH solution (Rotation speed: 1600 rpm, Scan rate: 10 mV s^{-1}), respectively.

analysis was carried out on an Elementar Analysensysteme GmbH Vario EL.

2.4. Electrochemical measurements

The as-prepared catalyst samples (7.0 mg) were dispersed in a mixture of ethanol (350.0 μL), and 5 wt% Nafion solution (95.0 μL)

by using an ultrasonic cleaner (VGT-1860QTD) with 150 W for 1 h. The catalyst ink (5.0 μL) was spread on a *glassy carbon* (GC) disk electrode (5.0 mm in diameter), and then dried in an oven at 40 °C for 120 min. For comparison, 10.0 mg commercial Pt/C catalyst (20 wt.% Pt, E-TEK) was ultrasonically dispersed in the solution of 1.80 mL ethanol and 0.20 mL Nafion solution (5 wt.%) for 1 h, and 6.0 μL of the above obtained suspension was dropped onto the surface of the GC disk electrode with a catalyst loading of 30 μg Pt cm^{-2}.

Rotating disk electrode (RDE) and *cyclic voltammetry* (CV) experiments (Auto84480 instrument) were performed in 0.1 mol L^{-1} KOH electrolyte with an Ag/AgCl electrode in saturated KCl solution, which potential was −0.198 V (*vs.* standard hydrogen electrode) as a reference electrode, a Pt foil as a counter electrode, and the GC disk electrode coated with catalyst thin film as a working electrode. For CV and RDE tests, oxygen or nitrogen (100 sccm) was continuously purged into the electrolyte for at least 30 min. In the RDE test, the working electrode was rotated with variable rotating speeds of 400–2000 rpm. For both RDE and CV tests, the potential range was from −0.8 to 0.2 V (*vs.* Ag/AgCl) with a scan rate of 10 mV s^{-1}. Electrode kinetic data were calculated according to the well-known *Koutecky-Levich* (K-L) equation:

$$i - 1 = ik - 1 + il - 1 \tag{1}$$

$$i_L = 0.620 nFAD_O^{2/3} w^{1/2} v^{-1/6} C_{O_2} = Bw^{1/2} \tag{2}$$

Table 1
Pore structure parameters of LHNPC-x.

Samples	BET Surface Area (m^2 g^{-1})	Pore Volume (cm^3 g^{-1})	Micropore Area (m^2 g^{-1})
LNHPC-800	1049	0.4	780
LNHPC-900	1577	0.5	976
LNHPC-1000	2986	0.3	564

Table 2
The nitrogen species and their corresponding content percentage of LNHPC-x.

Samples	Pyridinic N(%)	Pyrrolic N(%)	Graphitic N(%)	Oxidized N(%)
LNHPC-800	35.2	32.4	16.7	15.7
LNHPC-900	38.5	31.4	24.5	5.6
LNHPC-1000	15.8	20.7	63.5	0
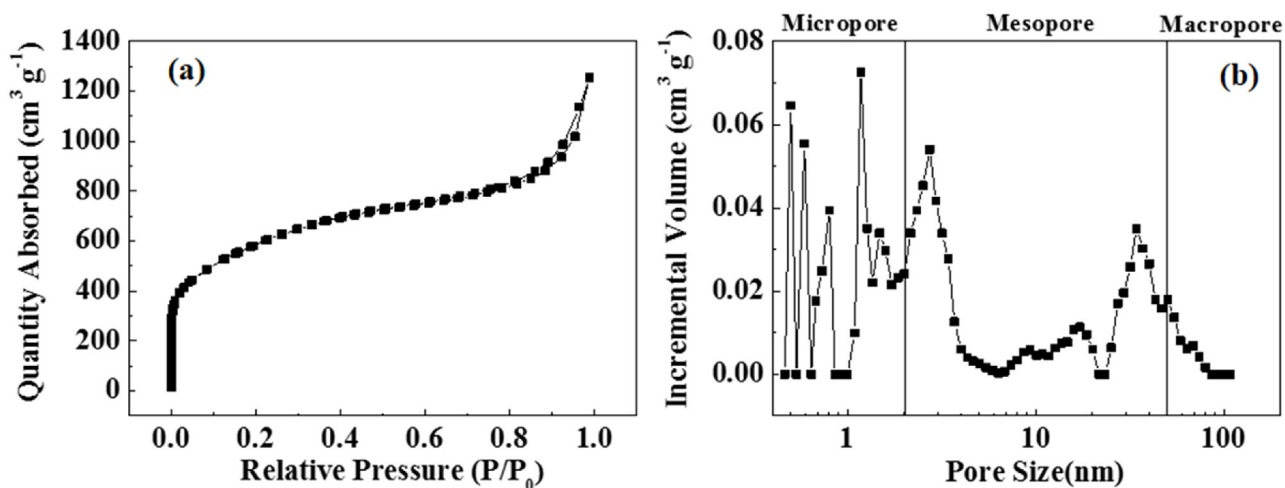
Fig. 7. N$_2$ adsorption-desorption isotherms (a), and the pore size distribution of DFT model (b) of LHNHPC.
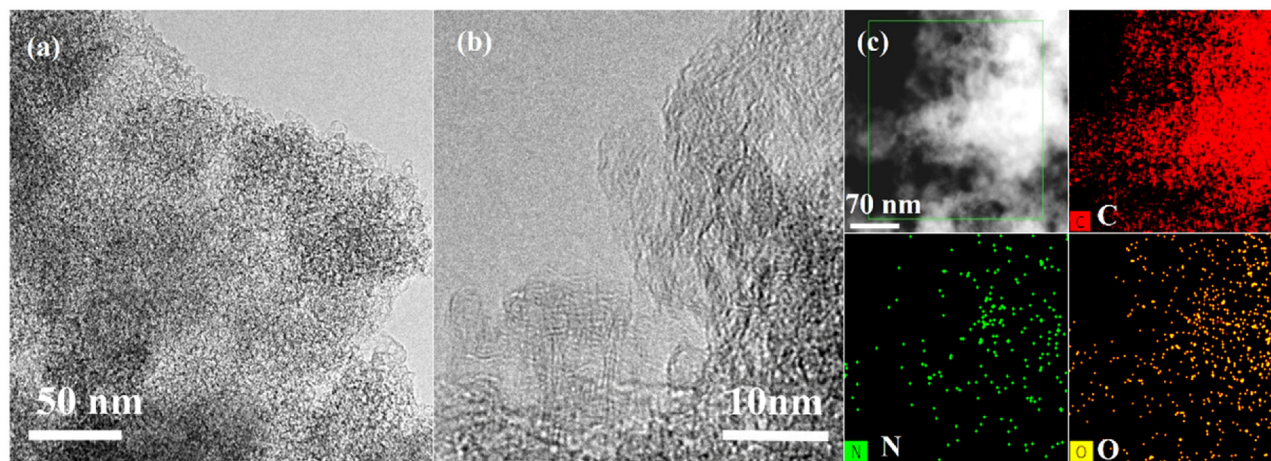
Fig. 8. The TEM images of LHNHPC, (a) and (b); STEM and the element mapping images of LHNHPC (c).

Table 3
The nitrogen weight content percentage of LNHPC-1000 and LNHPC-1000 after the hydrothermal treatment in NH$_3$·H$_2$O at 180 °C for 12 h (LHNHPC) by elemental analysis.

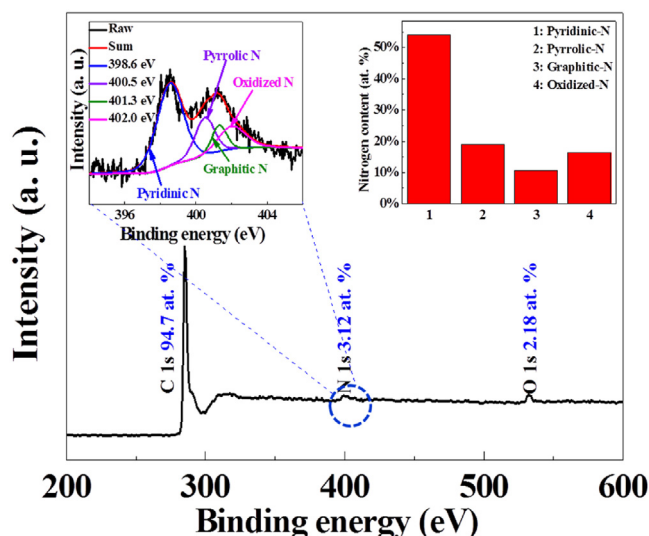| Sample	Weight (mg)	C (wt.%)	H (wt.%)	N (wt.%)
LNHPC-1000	1.8280	89.68	1.136	1.070
LHNHPC	1.8530	87.60	1.310	3.340

Fig. 9. XPS survey spectra of LHNHPC. The inset shows the nitrogen species and the corresponding nitrogen (at.%) for LHNHPC.

Fig. 10. CV curves of LHNHPC and LNHPC-1000 in N_2 (dash line) and O_2-(solid line) saturated 0.1 mol L^{-1} KOH solution at a scan rate of 10 mV s^{-1}.

where i is the measured current density, i_L the diffusion-limited current density, i_k the kinetic current density, ω the angular velocity of the rotating electrode, F the Faraday constant (96,485 C mol^{-1}), D_0 the diffusion coefficient of oxygen in 0.1 mol L^{-1} KOH ($D_0 = 1.9 \times 10^{-5}$ cm^2 s^{-1}), υ the kinetic viscosity (0.01 cm^2 s^{-1}), and C_0 the bulk concentration of oxygen (1.2×10^{-6} mol cm^{-3}). The electron transfer number (n) and kinetic current density (i_k) are extracted from the slopes and the intercepts of the linear K-L plots, respectively.

The electron transfer number (n), as well as the HO_2^- intermediate production percentage (%HO_2^-), can also be obtained from the *rotating ring-disk electrode* (RRDE) voltammograms, using the following equations:

$$n = \frac{4 * I_D}{I_D + I_R/N} \tag{3}$$

$$\%_{HO_2} = \frac{4 - n}{2} \tag{4}$$

Here, I_d is the disk current, I_R the ring current, and N the current collection efficiency of the Pt ring (0.37).

The methanol tolerance test was carried out in O_2-saturated 0.1 mol L^{-1} KOH solution with or without 0.5 mol L^{-1} CH_3OH by using the CV technique. The accelerated aging tests were performed in O_2-saturated 0.1 mol L^{-1} KOH solution by the aid of the CV technique.

The accelerated aging was obtained by 10,000 potential cycles from 0.6 V to 1.0 V (*vs.* RHE) at a rate of 50 mV s^{-1} [53,54]. It should be noted that without specification, all the potential are referred to the RHE.

3. Results and discussion

3.1. Morphology and material structure

According to the scheme shown in Fig. 1, LNHPC-x was firstly synthesized by a modified classical sol-gel-preparation method, with $(NH_4)_2CO_3$ as the catalyst of the polymerization and pore-forming material due to the fact that it is easy to be decomposed to produce some gas during the pyrolysis process, and NH_3 as the N precursors and activating agent. The typical SEM and TEM images of LNHPC-x are displayed in Fig. 2.
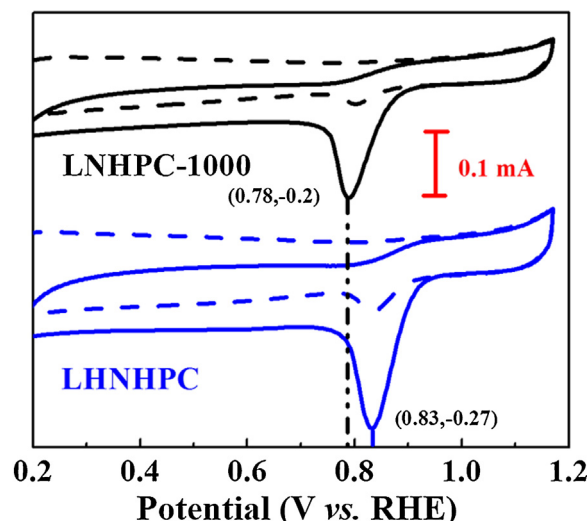
With the pyrolysis temperature increasing, one can intuitively find that the particles gradually become larger, and finally form a sheet structure as marked by the circle with dashed line in Fig. 2c. Besides, the TEM images show that a large amount of micropores are formed with the NH_3-activating temperature enhancing.

In order to investigate the pore structure of the LNHPC-x, the N_2 adsorption-desorption isotherms of the samples were recorded (Fig. 3). Typical IV N_2 adsorption/desorption isotherms with distinct hysteretic loops indicate the mesoporous structure of the as-prepared samples (Fig. 3a). Also, their corresponding pore size distributions show the coexistence of micropores, mesopores, and large-mesopores (Fig. 3b). This result indicates that the hierarchically porous structure has been successfully fabricated, which could shorten the pathway of mass transfer and be favorable for ORR due to the accessibility to active sites. The corresponding BET surface area and total pore volume of these three samples are found to be 1049 m^2 g^{-1} and 0.4 cm^3 g^{-1} (LNHPC-800), 1577 m^2 g^{-1} and 0.5 cm^3 g^{-1} (LNHPC-900), and 2986 m^2 g^{-1} and 0.3 cm^3 g^{-1} (LNHPC-1000) (Table 1).

Additionally, it can be found that LNHPC-1000 possesses the largest BET but the smallest micropore area (564 m^2 g^{-1}), which may be caused by the fact that although exorbitant NH_3-activating temperature leads to more micropores, abundant cross-linking micropores could be evolved into mesopores. It can also be identified by the corresponding pore size distribution (Fig. 3b). According to the intensity ratio (I_D/I_G) of D-band ($\sim$1330 cm^{-1}) to G-band ($\sim$1580 cm^{-1}) in the Raman spectra (Fig. 4), LNHPC-1000 has a higher I_D/I_G ratio compared with LNHPC-800 and LNHPC-900. This indicates higher defect densities in the graphitic carbon structure as the ammoniating temperature increases, which are crucial for enhancing ORR activity [55].

In order to clarify the bonding configuration of nitrogen dopants in LNHPC-x, XPS measurements were conducted. According to the XPS survey scan and analysis (Fig. 5a), the total nitrogen content for LNHPC-800, LNHPC-900, and LNHPC-1000 are decreasing gradually from 3.23 at.% (LNHPC-800) to 1.29 at.% (LNHPC-1000).

The high-resolution XPS spectra of N1s are deconvoluted into four sub-peaks, including pyridinic-N (398.6 eV), pyrrolic-N (400.5 eV), graphitic-N (401.3 eV), and oxidized-N (402.0 eV) for both LNHPC-800 and LNHPC-900 (Fig. 5b and c). While, in the case of LNHPC-1000 (Fig. 5d), the graphitic-N becomes the dominants in the various types of N dopants due to the fact that graphitic-N is more stable than pyridinic-N, pyrrolic-N and oxidized-N during the
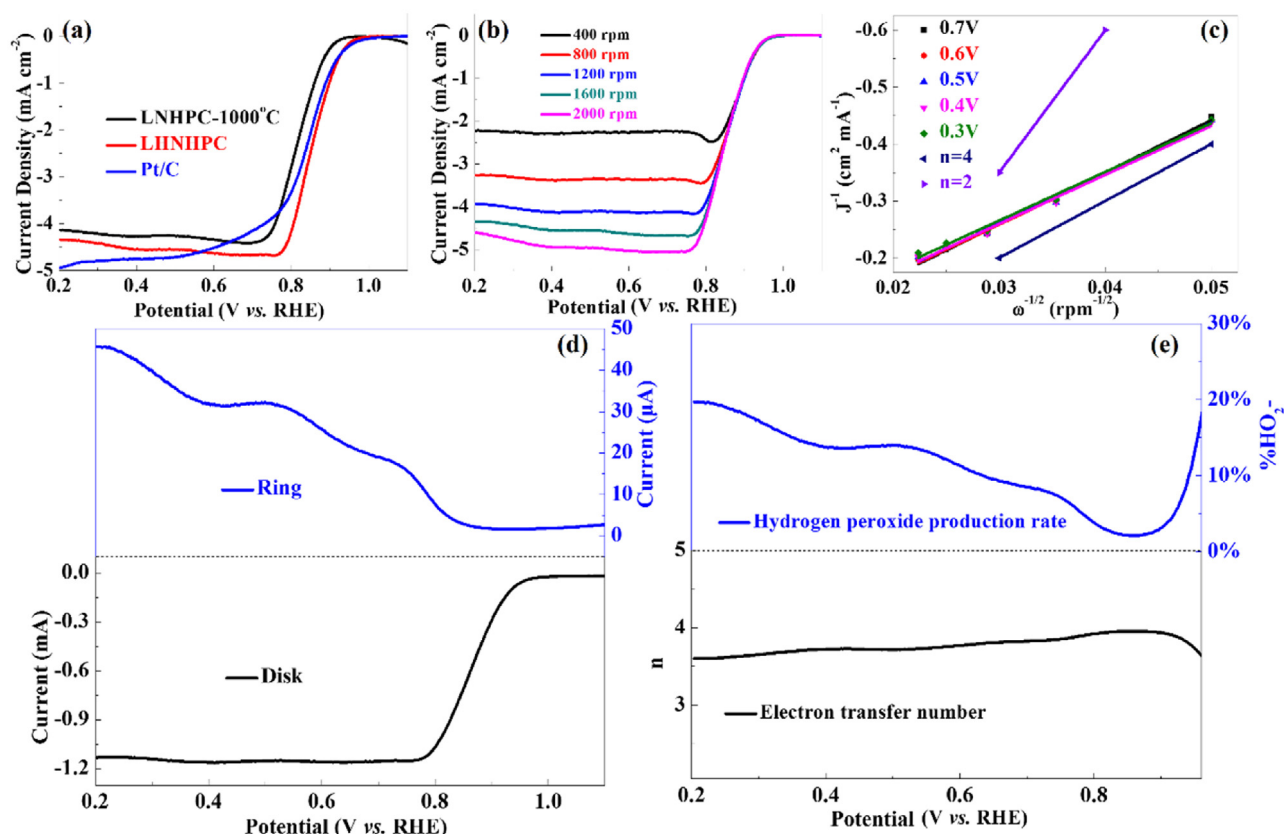
Fig. 11. Electrocatalytic ORR results in O_2-saturated 0.1 mol L^{-1} KOH. (a) RDE polarization curves of LNHPC, LHNHPC, and Pt/C at 10 mV s^{-1} and 1600 rpm; (b) RDE polarization curves of LHNHPC at different rotating speeds; (c) The Koutecky-Levich plots for LHNHPC obtained from the RDE results; (d) RRDE voltammograms in an O_2-saturated 0.1 mol L^{-1} KOH solution at room temperature (rotation speed: 1600 rpm, scan rate: 10 mV s^{-1}) for LHNHPC, and (e) Electron transfer number and hydrogen peroxide yield obtained from the RRDE curves for LHNHPC.

Table 4
Summary of reported ORR performance of metal-free electrocatalysts. All catalysts were tested in 0.1 M KOH.

Catalyst	Half-wave potential (V vs. NHE)	Limiting current density (mA/cm²)	Scanning rate/Rotation rate (mV/s)/(rpm)	References
N-doped mesoporous carbon	0.82	~6.3	10/1600	J. Am. Chem. Soc. 133 (2010) 206
N-doped nanoporous carbon	0.77	4.8	20/1600	Energy Environ. Sci. 7 (2014) 4095
Porous doped carbon nanofibers	0.80	5.6	10/1600	J. Am. Chem. Soc. 136 (2014) 14385
3D N and P co-doped mesoporous nanocarbon foams	0.85	~4.5	5/1600	Nat. Nanotechnol. 48 (2015) 444
N-doped porous carbon nanosheets	0.76	~5.8	10/1600	Adv. Mater. 28 (2016) 5080
Nitrogen-doped hierarchically porous carbon	0.85	~5.8	10/1600	Nat. Commun., 5 (2014) 4973
BCN graphene	0.72	~5.5	10/1600	Angew. Chem. Int. Ed. 51 (2012) 4209
LHNHPC	**0.86**	**~4.4**	**10/1600**	**This work**
Pt/C (20 wt%)	**0.85**	**~4.9**	**10/1600**	**This work**

exorbitant ammoniating temperature treatment. The summarized data for these nitrogen dopants are listed in Table 2.

It should be noted that a dramatic decrease in the pyridinic-N content could be resulted from the enhanced pyrolysis temperature. Although LNHPC-1000 possesses the lowest N content (1.29 at.%), the highest defect densities and largest BET surface area could be well acknowledged to enhance ORR activity.

The similar ORR activity of LNHPC-x samples could be obtained in terms of almost the same onset potentials and diffusion-limiting current density in LSV curves with RDE measurements in an O_2-saturated 0.1 mol L^{-1} KOH solution (Fig. 6). This phenomenon may be due to an optimal balance among porosity, defects and content of N in these three samples.

Based on the above results, one can find that LNHPC-1000 has a desirable structure of a higher I_D/I_G ratio, and suitable pore distribution for enough active sites and better mass transfer channels

with respect to LNHPC-800 and LNHPC-900. While its N content is quite low, with only 1.29 at.%. As known, N content also plays a very important role in enhancing the ORR activity of carbon-based materials. Accordingly, in order to optimize ORR performance of the catalyst, LNHPC-1000 was chosen as basement to make further effort to increase its N content by the hydrothermal process in $NH_3 \cdot H_2O$.

After the further treatment through the hydrothermal process in $NH_3 \cdot H_2O$, the obtained LHNHPC has a typical IV nitrogen adsorption/desorption isotherm with distinct hysteretic loops (Fig. 7), indicating its mesoporous structure. The BET surface area of LHNHPC gets to 2600 cm² g^{-1} that is almost no change with respect to that of LNHPC-1000 (2986 cm² g^{-1}). Simultaneously, the corresponding pore size distribution of LHNHPC still exhibits the coexistence of micropores, mesopores, and large-mesopores, with-
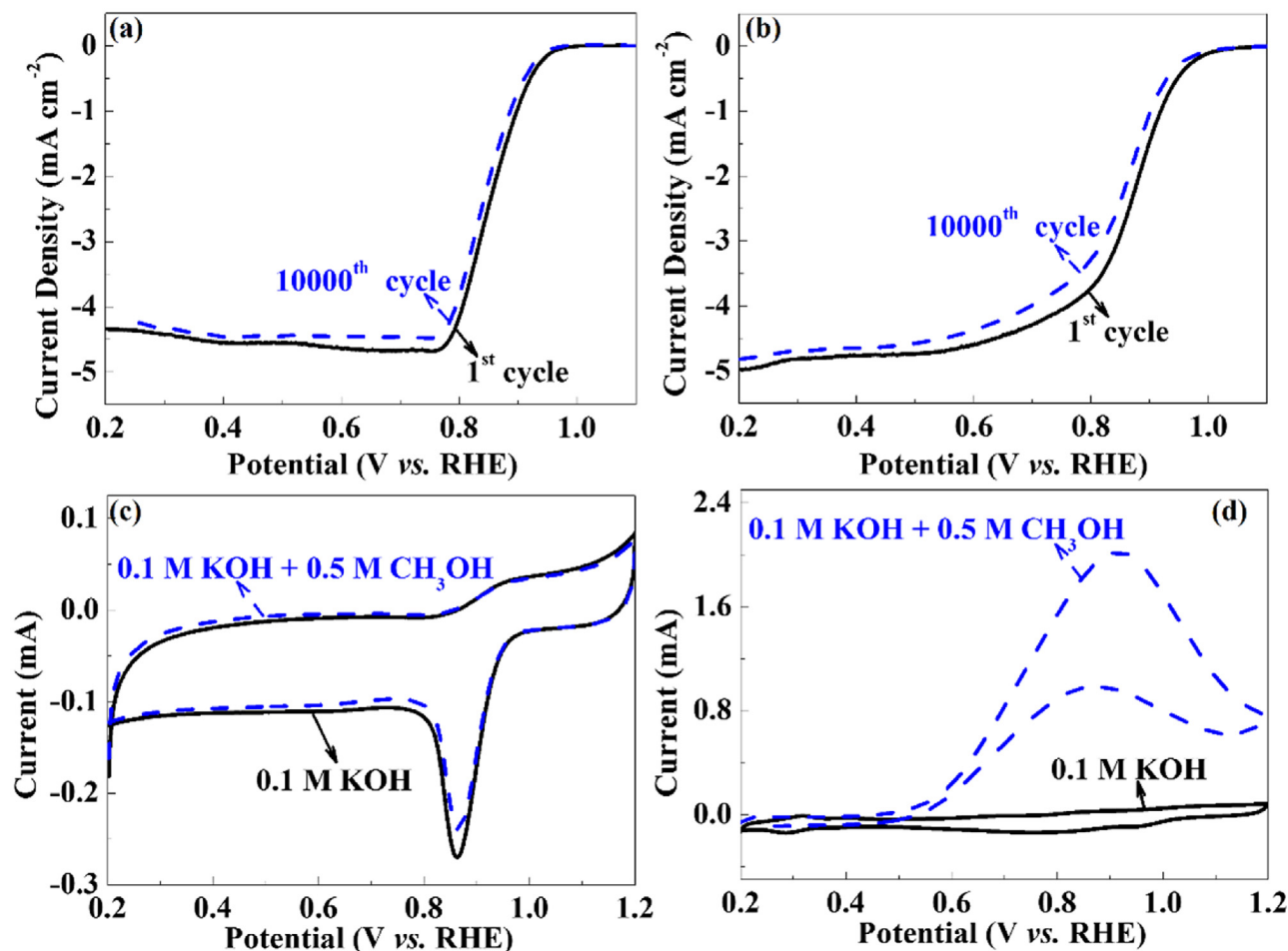
Fig. 12. RDE voltammograms of the LHNHPC (a) and commercial Pt/C (b) before and after 10,000 potential cycles between 0.6 V–1.0 V (*vs.* RHE) at 50 mV s^{-1} in an O$_2$-saturated 0.1 mol L^{-1} KOH solution; Cyclic voltammograms of the LHNHPC (c), and commercial Pt/C (d) in an O$_2$-saturated 0.1 mol L^{-1}L KOH solution at room temperature with and without 0.5 mol L^{-1} methanol.

out obvious change in the pore size distribution by comparing the results as shown in Figs. 3 b and 7b.

The porous and loose structure of LHNHPC can be verified by TEM images (Fig. 8a and b). STEM image and corresponding element mappings (Fig. 8c) show the fog-like structure of the LHNHPC and uniform dispersion of C, N, and O elements, respectively.

As it can be noticed from XPS results (Fig. 9), a high N doping level of 3.12 at.% is achieved for LHNHPC with the hydrothermal reaction of aqueous ammonia of LNHPC-1000 (1.29 at.% N). This can also be confirmed from the elemental analysis results, with the content of N obviously increasing from 1.07 wt.% (LNHPC-1000) to 3.34 wt.% (LHNHPC) after the NH$_3$·H$_2$O hydrothermal treatment at 180 °C for 12 h (Table 3). In addition, the relative ratio of pyridinic N, which is well acknowledged as the active site for ORR, is also increased in some extent (the inset of Fig. 9).

Those above characterizations about LHNHPC can guarantee that the morphology and pore structure remains almost unchanged except for the increased N content compared with that of LNHPC-1000.

3.2. Electrochemical analysis

To evaluate the ORR activities of LNHPC-1000 and LHNHPC, cyclic CV measurements were initially performed and the results are shown in Fig. 10. In the N$_2$-saturated 0.1 mol L^{-1} KOH solution, both samples display featureless CV curves, while they give a well-defined ORR peak in O$_2$-saturated 0.1 mol L^{-1} KOH solu-

tion. Comparatively, the CV curve for the LHNHPC shows a distinct reduction peak at 0.83 V, corresponding to the ORR, with an obvious positive shift for the onset potential with respect to that on the LNHPC-1000.

RDE measurements were then used to further compare the activity and reaction mechanism of ORR of different catalysts (Fig. 11). For comparison, a commercial Pt/C (20 wt.% Pt, E-TEK) were also tested under identical conditions. It is clear that the ORR onset potential of LHNHPC (0.98 V) shifts significantly in the positive direction relative to that of LNHPC-1000 (0.94 V), and almost matches well with that of the Pt/C (0.98 V) (Fig. 11a). This ORR activity is among the highest reported on metal-free electrocatalysts in basic media (Table 4). This behavior could be explained that the more N-doping contents for the LHNHPC lead to more active sites (pyridinic N) with respect to that of the LNHPC-1000. Moreover, the desirable ORR performance at LHNHPC could be due to the combined effect of its large specific surface area, abundant active sites for ORR (Pyridinic N), and hierarchical porous structure with a multimodal pore distribution for rapid mass transfer of reactants, products, and the electrolyte.

In order to get a deep insight into the ORR mechanism of the LHNHPC, a set of polarization curves was recorded on the RDE at different rotating speeds (Fig. 11b). The linearity of the K-L plots and the near parallelism of the fitting lines (Fig. 11c) suggest a first-order reaction kinetics with respect to the concentration of dissolved O$_2$ and similar electron transfer number for ORR at different potentials. The highly parallelism of the plots of LHNHPC to

the line representing for theoretical 4e$^-$ transfer process of ORR indicates that its n value approaches 3.75, very close to 4 of the Pt/C catalyst. To further investigate the ORR catalytic pathway at LHNHPC, the RRDE technique was employed, in which the amount of H_2O_2 generated at the disk electrode could be accurately determined by the ring current. As shown in Fig. 11d and e, in the potential range of 0.2 V–1.0 V, the measured values of H_2O_2 yield are below ~20%, reflecting an electron transfer number of 3.6–4.0, and suggesting that its ORR process inclines to high 4e$^-$ selectivity. These results are in accordance with the RDE measurements at different rotation speeds, indicating the high-efficiency 4e$^-$ ORR electrocatalytic activity of LHNHPC.

To authenticate the factors, which have influence on the ORR activities of the catalysts, the following brief discussions are presented. Obviously, the significantly boosted ORR activities of LHNHPC over its raw counterparts (LNHPC-1000) clearly exemplify the critical role of nitrogen dopants [56]. On the other hand, the lower N content in LNHPC-1000 does not lead to a commensurate drop in ORR activity, indicating that the ORR activity is not only correlated to the content of N dopants but also related to the defect densities, the graphitic degree (rapid electron transfer rate) and specific surface area (exposed active sites and accessible surface area for mass transfer, *e.g.* O_2 and electrolyte) of the samples, which could be justified by the electrochemical results (Fig. 6) [57].

The durability of the LHNHPC catalyst was assessed by using the accelerated durability test protocol of the US Department of the Energy by cycling the catalysts between 0.6 V and 1.0 V at 50 mV s^{-1} under O_2 atmosphere. As it can be seen from Fig. 12a, after 10,000 continuous potential cycles, the half-wave potential $E_{1/2}$ exhibits a small negative shift of ~12 mV at the LHNHPC catalyst, which is almost the same as that at the commercial Pt/C catalyst (~12 mV; see Fig. 12b).

The as prepared LHNHPC catalyst was also exposed to fuel molecules for testing the poisoning effects. For DMFCs, it is highly desirable that ORR catalysts exhibit high tolerance to methanol that can pass across the electrolyte membrane from the anode to the cathode (methanol crossover). The CV curves depicted in Fig. 12c and d were obtained in O_2-saturated 0.1 mol L^{-1} KOH solution with 0.5 mol L^{-1} methanol. It can be clearly seen that there is no obvious change in the ORR current density of LHNHPC after the addition of methanol. However, the Pt/C catalyst shows a sharp jump in the CV curve due to the methanol oxidation reaction. These results suggest that LHNHPC has a much higher catalytic selectivity toward the ORR in the simultaneous presence of O_2 and CH_3OH than the commercial Pt/C. These results unambiguously disclose that LHNHPC possesses desirable long-term durability, high selectivity towards 4e$^-$ ORR, and excellent methanol tolerance with respect to Pt/C, which makes it highly promising as a Pt-substitute ORR electrocatalyst for FCs practical applications.

4. Conclusions

In summary, a new type of metal-free ORR electrocatalyst by a modified classical sol-gel-preparation method was developed; it possesses large specific surface area, high content N dopants, 3D cross-linking hierarchically porous structure. LHNHPC showed high electrocatalytic activity towards ORR, long-term stability, and excellent methanol tolerance compared with the commercial Pt/C catalyst. It has been identified that large specific surface area, hierarchical porous structure and rich nitrogen doping are the key factors in achieving the high ORR performance. It is expected that further study of the present synthesis process may result in scalable mass production of non-precious metal catalysts for a broad range of electrochemical devices.

References

[1] A.S. Arico, P. Bruce, B. Scrosati, J.M. Tarascon, W.V. Schalkwijk, Nat. Mater. 4 (2005) 366–377.
[2] B.C.H. Steele, A. Heinzel, Nature 414 (2001) 345–352.
[3] N.S. Lewis, D.G. Nocera, Proc. Natl. Acad. Sci. U. S. A. 103 (2006) 15729–15735.
[4] P.G. Bruce, S.A. Freunberger, L.J. Hardwick, J.M. Tarascon, Nat. Mater. 11 (2011) 19–29.
[5] E.E. Benson, C.P. Kubiak, A.J. Sathrum, J.M. Smieja, Chem. Soc. Rev. 38 (2009) 89–99.
[6] J. Suntivich, H.A. Gasteiger, N. Yabuuchi, H. Nakanishi, J.B. Goodenough, S.H. Yang, Nat. Chem. 3 (2011) 546–550.
[7] Y. Liang, H. Wang, J. Zhou, Y. Li, J. Wang, T. Regier, H. Dai, J. Am. Chem. Soc. 134 (2012) 3517–3523.
[8] F.C. Vallejo, M.T.M. Koper, A.S. Bandarenka, Chem. Soc. Rev. 42 (2013) 5210–5230.
[9] H. Wang, Y. Liang, Y. Li, H. Dai, Angew. Chem. Int. Ed. 50 (2011) 10969–10972.
[10] S. Zhao, H. Yin, L. Du, L. He, K. Zhao, L. Chang, G. Yin, H. Zhao, S. Liu, Z. Tang, ACS Nano 8 (2014) 12660–12668.
[11] A. Holewinski, J.C. Idrobo, S. Linic, Nat. Chem. 6 (2014) 828–834.
[12] W. Cheng, R.G. Compton, Angew. Chem. Int. Ed. 54 (2015) 7082–7085.
[13] Z. Li, G. Li, L. Jiang, J. Li, G. Sun, C. Xia, F. Li, Angew. Chem. Int. Ed. 54 (2015) 1494–1498.
[14] M.S. Faber, S. Jin, Energ. Environ. Sci. 7 (2014) 3519–3542.
[15] M.K. Debe, Nature 486 (2012) 43–51.
[16] M.R. Gao, J. Jiang, S.H. Yu, Small 8 (2012) 13–27.
[17] A.S. Aricò, S. Srinivasan, V. Antonucci, Fuel Cells 1 (2001) 133–161.
[18] S. Song, V. Maragou, P. Tsiakaras, J. Fuel Cell Sci. Technol. 4 (2007) 203–209.
[19] G. Wu, K.L. More, C.M. Johnston, P. Zelenay, Science 332 (2011) 443–447.
[20] K. Parvez, S. Yang, Y. Hernandez, A. Winter, A. Turchanin, X. Feng, K. Müllen, ACS Nano 6 (2012) 9541–9550.
[21] L. Li, S.H. Chai, S. Dai, A. Manthiram, Energ. Environ. Sci. 7 (2014) 2630–2636.
[22] C. Erbay, X. Pu, W. Choi, M.J. Choi, Y. Ryu, H. Hou, F. Lin, P.D. Figueiredo, C. Yu, A. Han, J. Power Sources 280 (2015) 347–354.
[23] S.W. Jee, W. Choi, C.H. Ahn, G. Yang, H.K. Cho, J.H. Lee, C. Yu, J. Mater. Chem. A 3 (2015) 13767–13775.
[24] G. Yang, W. Choi, X. Pu, C. Yu, Energ. Environ. Sci. 8 (2015) 1799–1807.
[25] J. Liang, R.F. Zhou, X.M. Chen, Y.H. Tang, S.Z. Qiao, Adv. Mater. 26 (2014) 6074–6079.
[26] S. Wang, E. Iyyamperumal, A. Roy, Y. Xue, D. Yu, L. Dai, Angew. Chem. Int. Ed. 50 (2011) 11756–11760.
[27] L. Yang, S. Jiang, Y. Zhao, L. Zhu, S. Chen, X. Wang, Q. Wu, J. Ma, Y. Ma, Z. Hu, Angew. Chem. Int. Ed. 50 (2011) 7132–7135.
[28] S. Brouzgou, S. Song, Z.-X. Liang, P. Tsiakaras, Catalysts 6 (2016) 159.
[29] K. Wan, G.-F. Long, M.-Y. Liu, L. Du, Z.-X. Liang, P. Tsiakaras, Appl. Catal. B: Environ. 165 (2015) 566–571.
[30] T. Jiang, Y. Wang, K. Wang, Y. Liang, D. Wu, P. Tsiakaras, S. Song, Appl. Catal. B: Environ. 189 (2016) 1–11.
[31] Y. Hua, T. Jiang, K. Wang, M. Wu, S. Song, Y. Wang, P. Tsiakaras, Appl. Catal. B: Environ. 194 (2016) 202–208.
[32] G.-F. Long, X.-H. Li, K. Wan, Z.-X. Liang, J.-H. Piao, P. Tsiakaras, Appl. Catal. B: Environ. 203 (2017) 541–548.
[33] H. Tang, Y. Zeng, Y. Zeng, R. Wang, S. Cai, C. Liao, H. Cai, X. Lu, P. Tsiakaras, Appl. Catal. B: Environ. 202 (2017) 550–556.
[34] Y. Li, Y. Zhao, H. Cheng, Y. Hu, G. Shi, L. Dai, L. Qu, J. Am. Chem. Soc. 134 (2012) 15–18.
[35] D. Geng, Y. Chen, Y. Chen, Y. Li, R. Li, X. Sun, S. Ye, S. Knights, Energ.Environ. Sci. 4 (2011) 760–764.
[36] Z. Yang, Z. Yao, G. Li, G. Fang, H. Nie, Z. Liu, X. Zou, X. Chen, S. Huang, ACS Nano 6 (2012) 205–211.
[37] J. Liang, Y. Zheng, J. Chen, J. Liu, D.H. Jurcakova, M. Jaroniec, S.Z. Qiao, Angew. Chem. Int. Ed. 51 (2012) 3892–3896.
[38] W. Xia, J. Masa, M. Bron, W. Schuhmann, M. Muhler, Electrochem. Commun. 13 (2011) 593–596.
[39] W. Yang, T.P. Fellinger, M. Antonietti, J. Am. Chem. Soc. 133 (2011) 206–209.
[40] G. Ma, R. Jia, J. Zhao, Z. Wang, C. Song, S. Jia, Z. Zhu, J. Mater. Chem. C 115 (2011) 25148–25154.
[41] S. Chen, J. Bi, Y. Zhao, L. Yang, C. Zhang, Y. Ma, Q. Wu, X. Wang, Z. Hu, Adv. Mater. 24 (2012) 5593–5597.
[42] B.Y. Guan, L. Yu, X.M. Lou, Adv. Mater. 28 (2016) 9596–9601.

[43] B.Y. Guan, L. Yu, X.M. Lou, J. Am. Chem. Soc. 138 (2016) 11306–11311.
[44] K. Gong, F. Du, Z. Xia, M. Durstock, L. Dai, Science 323 (2009) 760–764.
[45] K. Qu, Y. Zheng, S. Dai, S.Z. Qiao, Nanoscale 7 (2015) 12598–12605.
[46] L. Qu, Y. Liu, J.B. Baek, L. Dai, ACS Nano 4 (2010) 1321–1326.
[47] B.Y. Xia, Y. Yan, N. Li, H.B. Wu, X.W. Lou, X. Wang, Nat. Energy 1 (2016) 15006–15013.
[48] B.Y. Guan, L. Yu, X.M. Lou, Energ. Environ. Sci. 9 (2016) 3092–3096.
[49] J. Liang, Y. Jiao, M. Jaroniec, S.Z. Qiao, Angew. Chem. Int. Ed. 51 (2012) 11496–11500.
[50] Y. Hua, T. Jiang, K. Wang, M. Wu, S. Song, Y. Wang, P. Tsiakaras, Appl. Catal. B: Environ. 194 (2016) 202–208.
[51] H.W. Liang, X. Zhuang, S. Bruller, X. Feng, K. Mullen, Nat. Commun. 5 (2014) 4973–4979.
[52] W. Bak, H.S. Kim, H. Chun, W.C. Yoo, Chem. Commun. 51 (2015) 7238–7241.
[53] Y. Wang, S. Song, P.K. Shen, C. Guo, C.M. Li, J. Mater. Chem. 19 (2009) 6149–6153.
[54] W. Wei, H. Liang, K. Parvez, X. Zhuang, X. Feng, K. Mullen, Angew. Chem. Int. Ed. 53 (2014) 1570–1574.
[55] C. He, S. Song, J. Liu, V. Maragou, P. Tsiakaras, J. Power Sources 195 (2010) 7409–7414.
[56] S. Kattel, G. Wang, J. Mater. Chem. A 1 (2013) 10790–10797.
[57] L. Lai, J.R. Potts, D. Zhan, L. Wang, C.K. Poh, C. Tang, H. Gong, Z. Shen, J. Lin, R.S. Ruoff, Energ. Environ. Sci. 5 (2012) 7936–7942.